Scilight

Journal of Machine Learning and Information Security
https://www.sciltp.com/journals/jmlis

Article

Harmonic-Suppressed BR/HR Detection in FMCW Radar via Phase Correction with APSVD and VMD-Denoising

Yukun Huang [1,†], Denghao Li [1,†], Jingran Cheng [1], Haoming Feng [1], Min Duan [2], Junlin Yu [3], Jinqiu Zhou [3], Shengwei Liu [3], Zheng Wang [1], Yonghui Wu [1] and Huaqing Li [1,*]

[1] College of Electronic and Information Engineering, Southwest University, Chongqing 400715, China
[2] Chongqing Wukang Technology Co., Ltd., Chongqing 404100, China
[3] Hubei Edong Changjiang River Highway Bridge Co., Ltd., Huangshi 430000, China
* Correspondence: huaqingli@swu.edu.cn
† These authors contributed equally to this work.

How To Cite: Huang, Y.; Li, D.; Cheng, J.; et al. Harmonic-Suppressed BR/HR Detection in FMCW Radar via Phase Correction with APSVD and VMD-Denoising. *Journal of Machine Learning and Information Security* **2026**, 2(3), 14. https://doi.org/10.53941/jmlis.2026.100014

Received: 12 January 2026
Revised: 18 April 2026
Accepted: 22 April 2026
Published: 7 July 2026

Abstract: Radar has been used more and more in healthcare monitoring, so non-contact vital sign detection has received much attention. In real applications, it is still hard to separate heartbeat and respiration signals well because noise and respiratory harmonics often mix with weak heartbeat components. In this work, a vital signal enhancement and decomposition method for FMCW radar is presented. The method combines phase correction with a signal decomposition scheme based on adaptive projection singular value decomposition (APSVD) and variational mode decomposition (VMD) for denoising. First, chest motion is recovered from the phase of echo signals, and the phase-correction process improves signal quality. Then, APSVD is used to extract the respiration signal and suppress its harmonics. After that, VMD-based denoising is applied to the remaining signal so that the heartbeat signal can be separated more clearly. The experimental results show that the proposed method achieves an RMSE of 1.550827 bpm for breath rate (BR) estimation. For heart rate (HR) estimation, it obtains the lowest MAE and MRE among the compared methods, demonstrating improved average estimation accuracy while maintaining competitive RMSE performance.

Keywords: FMCW radar; vital signal separation; phase correction; decomposition based on APSVD and VMD-denoising; breath rate and heart rate estimation

1. Introduction

In recent years, the need for health monitoring and medical applications has continued to grow [1]. Because of this, mmWave radar sensors have been widely studied. They can be used in many non-contact sensing tasks, such as continuous blood pressure monitoring [2], sleep apnea detection [3,4], harmful action recognition [5], Ad hoc network enhancement [6], vital sign detection [7], and infant or child monitoring [8]. Among different physiological signals, respiration rate and heartbeat rate are two basic indicators of the human body's health condition [9]. So, a proper sensing device is important for non-contact vital sign detection.

FMCW radar [10–12] is suitable for this task because it has good range resolution and a high signal-to-noise ratio [13]. It can measure target information by using the frequency and phase differences between transmitted and reflected signals [14]. It also works with signal processing methods that help protect user privacy. For these reasons, FMCW radar is a useful choice for non-contact vital sign detection. Furthermore, FMCW radar can classify the acquired signals into multiple angular and range scales [15]. These advantages render FMCW radar particularly suitable for healthcare monitoring compared to other devices like unmodulated continuous wave (CW) radar [16], impulse radio ultra-wideband (IR-UWB) radar [17], video cameras [18], and audio equipment [19]. Notably, mmWave radar is applied to detect vital signs as a type of FMCW radar with a short wavelength, which offers significant advantages for the precise monitoring of subtle respiratory and cardiac movements [20]. To accurately obtain vital

signals in complex environments, it is essential to recover the mechanical signals of thoracic cavity movement from echo signals and represent them in terms of phase variation [21].

Since the respiration and heartbeat signals need to be extracted from the mechanical signal of thoracic cavity movement, a range of methods has been developed, including those utilizing wavelet transforms (WT) [22,23], deep learning techniques [24–27], and various signal decomposition algorithms [28–33]. Several methods have been used for vital sign extraction. One common method is wavelet transform (WT). WT gives high resolution in both the time domain and the frequency domain, so it can be used in vital signal analysis. But WT-based methods often need a reference signal. In practice, it is not easy to choose a proper adaptive wavelet template for different people. Deep learning methods [27] have also been used in this field. But these methods usually need a large amount of training data and long training time. This makes fast signal acquisition and real-time processing more difficult.

Signal decomposition methods have been widely used to separate respiration and heartbeat signals in recent years. EMD [28] can adaptively decompose a signal into several intrinsic mode functions by using local signal features, so it can be used for respiration and heartbeat separation. But it still suffers from mode mixing, endpoint effects, and sensitivity to noise. These problems become more serious when the signal is non-stationary. EEMD [31] reduces mode mixing by adding Gaussian white noise, but it may bring reconstruction errors. CEEMDAN [32] improves this process by using adaptive noise, and it can improve reconstruction accuracy and reduce the computational load. But EEMD and CEEMDAN still have difficulty in separating heartbeat-related frequency components clearly from the intrinsic mode functions. VMD [33] decomposes the signal into several band-limited modes with given center frequencies. It reduces the bandwidth of each mode so that the modes are more independent in the frequency domain. Because of this, VMD has better noise resistance than EMD-based methods [34].

But harmonic interference is still a problem. The harmonics from respiration and heartbeat can have similar frequencies [35]. Although a bandpass filter can eliminate harmonics outside the heartbeat frequency range [20], it cannot remove harmonics within this specific frequency band. These difficulties pose a challenge in distinguishing between the heartbeat and respiration with normal signal processing methods. Additionally, parameters in the VMD algorithm, such as the decomposition number of modes $\boldsymbol{K}$ and the secondary penalty factor α, need to have distinct configurations due to different application scenarios.

To address the aforementioned challenges, an improved method of vital signal decomposition is utilized to extract respiration and heartbeat signals. To enhance the micro-movement features of vital signal, the phase correction method is designed. Then, the adaptive projection singular value decomposition (APSVD) based on signal energy ratio is applied to extract the respiration signal and its harmonics from the vital signal. Then, a heartbeat signal extracting method based on VMD-denoising which has the ability to decompose the noisy heartbeat signal into several distinct signals with their own features in the Fourier spectral domain and time domain is applied.

Finally, the reconstructed respiration and heartbeat waves will be given, and the BR as well as HR can be calculated. The contributions of this paper are outlined as follows:

- The proposed phase correction method combines phase difference, phase unwrapping, abrupt change points suppression and signal detrending to successfully suppress the unknown noises and enhance the vital signal.
- The APSVD extracts the respiration signal and harmonics which reduce the impact on the heartbeat signal. Meanwhile, the method obtains the raw heartbeat signal for the next extraction method.
- The VMD-denoising heartbeat extraction method not only achieves robust performance using a single set of parameters but also effectively suppresses noise frequencies surrounding the nominal heartbeat frequency.

The structure of this paper is as follows: The mmWave radar model is given in Section 2. The realization of vital signal enhancement and decomposition method is shown in Section 3. Section 4 provides a detailed demonstration of the method's effectiveness through experimental results. Finally, Section 5 presents the conclusion.

2. mmWave Radar Model

A mmWave radar TI IWR1642BOOST [36] and a DCA1000EVM [37] as a data capture card are employed. The radar module functioning within the 77-81 GHz frequency band can detect chest micro-movement and keep sampling rate suitable in slow-time dimension for vital sign detection.

The data acquisition and signal processing procedures are detailed in Appendix A.

Based on the analysis in Appendix A, the mixed echo signal in the time domain for a specific range bin n and continuous chirps can be expressed as

$$M(n,t) = \phi(n,t) = x_h(n,t) + x_b(n,t) + x_{\text{noise}}(n,t) + x_{\text{body}}(n,t) \tag{1}$$

where x_h represents the signal component due to heartbeat-induced chest displacement, x_b represents the respiration-

induced component, x_{noise} denotes various noise sources, and x_{body} accounts for reflections from the stationary human body and other low-frequency disturbances.

The analysis in this section shows that the heartbeat and respiration signals can be represented as phase modulations, as indicated in (1). But noise from different sources can reduce accuracy. So a robust decomposition method is needed.

3. Proposed Method

3.1. Human Body Detection

To localize the human subject, the fast Fourier transform (FFT) is applied to the fast-time dimension data of each digitized chirp, as shown in (A10) in Appendix A. A mean filter is applied to reduce clutter before peak-seeking. This process identifies the range bin index K where the human subject is located. Based on this index, Equation (A10) can be refined as

$$\begin{aligned} Y[K,m] &= Ae^{-j\left(2\pi f K T_f + \frac{4\pi}{\lambda} R(KT_f + mT_s)\right)} \\ &= Ae^{-j2\pi f K T_f} \cdot e^{-j\frac{4\pi}{\lambda} R(KT_f + mT_s)} \end{aligned} \tag{2}$$

In (2), the phase term is

$$\phi[K,m] = \frac{4\pi}{\lambda} R(KT_f + mT_s) \tag{3}$$

Thus, the mixed signal (1) can be expressed in discrete form as

$$M[K,m] = \phi[K,m] = x_h[K,m] + x_b[K,m] + x_{\text{noise}}[K,m] + x_{\text{body}}[K,m] \tag{4}$$

Based on the mixed signal equation derived above, the respiration and heartbeat signals can be extracted using subsequent processing methods.

3.2. Phase Correction

For a detected human subject within the range dimension, we extract the phase information from the specific range bin cell over the slow-time axis. As shown in Equation (4), the last two terms interfere with the extraction of breathing and heartbeat signals. In this part, the method aims to suppress or even eliminate the interference and enhance the vital signal.

3.2.1. Phase Difference

The displacements caused by respiration and heartbeat can be detected using (3). Phase difference analysis [38] is highly sensitive to detecting minute movements or displacements. This sensitivity is crucial in radar systems for detecting physiological signals such as breathing and heartbeat, which induce tiny movements typically in the millimeter range. Additionally, this method minimizes interference and errors from environmental changes, offering a more stable and accurate vital signal. Based on phase difference, the micro-change in phase $\Delta\phi[\mathrm{K}, i]$ can be obtained and expressed as

$$\Delta\phi[\mathrm{K}, i] = \phi[\mathrm{K}, i] - \phi[\mathrm{K}, i-1] \tag{5}$$

where $i = 2, 3, \ldots, M$, and M is the last chirp index.

3.2.2. Phase Unwrapping

After phase difference analysis, a phase unwrapping operation [39] is applied to recover the true phase information. The phase angle is defined from 0 to π in the first and second quadrants, while in the third and fourth quadrants, it is defined as $[-\pi, 0]$. However, phase changes often exceed the range of $[-\pi]$ to $[\pi]$ due to micro-movements caused by the human body. Therefore, the phase unwrapping method in MATLAB is employed to ensure phase continuity. The unwrapped phase $\Phi[i]$ can be expressed as

$$\Phi[i] = \text{unwrap}(\Delta\phi[\mathrm{K}, i]) \tag{6}$$

where $i = 1, 2, \ldots, M$.

3.2.3. Abrupt Change Points Suppression

Random body movements can introduce abrupt changes (outliers) in the phase signal, leading to distortion. To mitigate this, a Hampel-like filter [40] is employed. For each point $\Phi[i]$, a sliding window of width w centered at i is considered. The standard deviation in the window is written as $\sigma[i]$. If $|\Phi[i]|$ is greater than $t \cdot \sigma[i]$, this point is taken as an outlier. Here, t is set to 0.5 from empirical results. Then, this point is replaced by the median value in the window. At the beginning and the end of the sequence, the window size is reduced to avoid crossing the boundary. The value of w is set to 5 because it works well for both noise suppression and signal preservation. The operation can be summarized as

$$\Phi[i] = \begin{cases} \text{median}\left(\Phi\left[i - \lfloor w/2 \rfloor : i + \lfloor w/2 \rfloor\right]\right), & \text{if } |\Phi[i]| > 0.5 \cdot \sigma[i] \\ \Phi[i], & \text{otherwise} \end{cases} \tag{7}$$

where $\sigma[i]$ is the standard deviation within the window. This step removes abrupt spikes and keeps the main physiological waveform.

3.2.4. Signal Detrending

The radar signal often contains baseline drift. This drift comes from temperature changes, humidity, circuit effects, and slight body movements. So low-frequency components are added to the signal. These components can make respiration and heartbeat detection less accurate.

To deal with this problem, a detrending method based on ordinary least squares is used. It is used to estimate the baseline curve $T[i]$. Then the detrended signal is written as

$$X[i] = \Phi[i] - T[i] \tag{8}$$

where $i = 1, 2, \ldots, M$.

After detrending, the signal is more stable. Then it is used for respiration and heartbeat decomposition.

3.3. Vital Signal Decomposition Based on APSVD and VMD-Denoising

The complete process of decomposition method is illustrated in Figure 1.

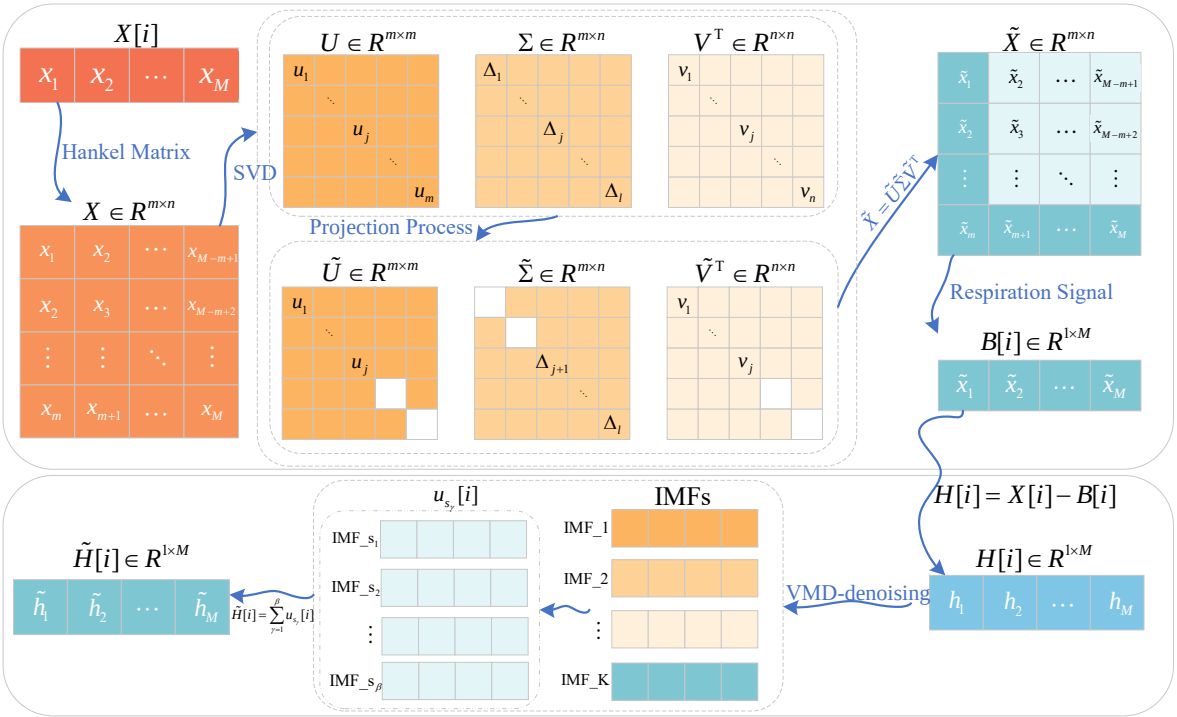

Figure 1. Flowchart of the decomposition method.

3.3.1. Respiration Signal Extraction and Harmonics Suppression

The vital signal contains both respiration and heartbeat components. The harmonics of the respiration signal may overlap with the heartbeat frequency band. So it is necessary to first extract the respiration signal and its harmonics.

Singular value decomposition (SVD) is used to separate signal components based on their energy [41]. A Hankel matrix is constructed from the time-series signal. Then SVD is applied to this matrix. The obtained singular values reflect the energy of different components. Larger singular values usually correspond to the respiration signal because it has higher energy. Smaller singular values are related to the heartbeat signal and noise.

APSVD is used to select the number of singular values automatically. This selection is based on the energy ratio between respiration and heartbeat. Then the respiration signal and its harmonics are extracted. At the same time, their influence on the heartbeat signal is reduced.

Consider a matrix $\boldsymbol{A} \in \boldsymbol{R}^{m\times n}$, where $m = \lfloor (M+1)/2 \rfloor$ and $n = M-m+1$. Its singular value decomposition (SVD) is written as

$$\boldsymbol{A} = \boldsymbol{U}\Sigma\boldsymbol{V}^{\mathrm{T}} \tag{9}$$

where $\boldsymbol{U} \in \boldsymbol{R}^{m\times m}$ and $\boldsymbol{V} \in \boldsymbol{R}^{n\times n}$. The matrix Σ is defined as

$$\Sigma = \begin{cases} (\mathrm{diag}(\Delta_1, \Delta_2, \cdots, \Delta_l), \boldsymbol{O}), & n \leqslant m \\ (\mathrm{diag}(\Delta_1, \Delta_2, \cdots, \Delta_l), \boldsymbol{O})^{\mathrm{T}}, & n > m \end{cases} \tag{10}$$

Here, $\Sigma \in \boldsymbol{R}^{m\times n}$ and $\boldsymbol{O}$ denotes an empty matrix. The parameter $l = \min(n, m)$. The singular values satisfy $\Delta_1 \geqslant \Delta_2 \geqslant \cdots \geqslant \Delta_l > 0$. Each $\Delta_i (i = 1, 2, \ldots, l)$ represents a singular value of $\boldsymbol{A}$.

To extract the respiration signal, the one-dimensional signal $X[i]$ is first converted into a Hankel matrix. Each column of this matrix is a time-shifted segment of the original signal. In this way, the time-series signal is transformed into a structured form. Then it can be processed by singular value decomposition.

$$\boldsymbol{X} = \begin{pmatrix} x_1 & x_2 & \cdots & x_{M-m+1} \\ x_2 & x_3 & \cdots & x_{M-m+2} \\ \vdots & \vdots & \ddots & \vdots \\ x_m & x_{m+1} & \cdots & x_M \end{pmatrix} \tag{11}$$

After the decomposition, the singular values are arranged in non-increasing order

$$\boldsymbol{\Delta} = (\Delta_1, \Delta_2, \cdots, \Delta_l), l = \min(n, m) \tag{12}$$

In addition, the magnitude of the singular values corresponds to the energy strength of the signal, allowing different signal components to be distinguished based on their varying energy levels.

Since the singular values corresponding to the respiration signal are generally greater than those of the heartbeat signal, the first 1 to j singular values are typically selected as features of the respiration signal based on empirical results. The remaining singular values are set to zero, which can be expressed as

$$\widetilde{\Sigma} = \begin{cases} (\mathrm{diag}(\Delta_1, \Delta_2, \cdots, \Delta_j), \boldsymbol{O}), & n \leqslant m \\ (\mathrm{diag}(\Delta_1, \Delta_2, \cdots, \Delta_j), \boldsymbol{O})^{\mathrm{T}}, & n > m \end{cases} \tag{13}$$

where j is an integer calculated adaptively based on the energy ratio of respiration to heartbeat. The whole steps of the calculation process can be expressed as

$$E_c = (\Delta_1^2, \Delta_1^2 + \Delta_2^2, \cdots, \Delta_1^2 + \Delta_2^2 + \cdots + \Delta_l^2) = (e_1, e_2, \ldots, e_l) \tag{14}$$

where E_c is cumulative energy. The total energy E is the last term of E_c. Then, the energy ratio E_r is obtained as

$$E_r = E_c/E = (\frac{e_1}{E}, \frac{e_2}{E}, \ldots, 1) \tag{15}$$

The energy threshold η is obtained adaptively as below

$$\eta = \frac{P_r}{P_r + P_h} \tag{16}$$

where P_r is the max amplitude limited to [0.1, 0.5] Hz [39] of the detrended vital signal $X[i]$, and P_h is the max amplitude limited to [1.0, 1.8] Hz [42]. The selection of j is defined as

$$j = \min\left\{ j \mid \frac{e_j}{E} \geq \eta \right\} \tag{17}$$

Correspondingly, the diagonal of left-singular matrix $\boldsymbol{U}$ is set to zero from $j+1$ to m, and the diagonal of right-singular matrix $\boldsymbol{V}$ is set to zero from $j+1$ to n. The modified matrices are defined as $\widetilde{\boldsymbol{U}}$ and $\widetilde{\boldsymbol{V}}$. The new Hankel matrix $\widetilde{\boldsymbol{X}}$ is obtained through the projection process as shown below

$$\widetilde{\boldsymbol{X}} = \widetilde{\boldsymbol{U}}\widetilde{\Sigma}\widetilde{\boldsymbol{V}}^{\mathrm{T}} \tag{18}$$

$$\widetilde{\boldsymbol{X}} = \begin{pmatrix} \tilde{x}_1 & \tilde{x}_2 & \cdots & \tilde{x}_{M-m+1} \\ \tilde{x}_2 & \tilde{x}_3 & \cdots & \tilde{x}_{M-m+2} \\ \vdots & \vdots & \ddots & \vdots \\ \tilde{x}_m & \tilde{x}_{m+1} & \cdots & \tilde{x}_M \end{pmatrix} \tag{19}$$

Finally, the respiration signal $B[i]$ can be extracted from $\widetilde{\boldsymbol{X}}$ as

$$B[i] = (\tilde{x}_1, \tilde{x}_2, \cdots, \tilde{x}_M) \tag{20}$$

3.3.2. Heartbeat Signal Extraction

The heartbeat signal is obtained by subtracting the extracted respiration signal from the composite signal, which corresponds to a time-domain signal cancellation process

$$H[i] = X[i] - B[i] \tag{21}$$

where $i = 1, 2, \ldots, M$. To accurately extract heartbeat signals, a method utilizing VMD for signal denoising is proposed.

VMD [33] decomposes an input signal into several band-limited modes. Each mode is characterized by a specific central frequency and is concentrated within a finite frequency band. The primary objective of VMD is to minimize the bandwidth of each mode, ensuring that the modes are as independent as possible in the frequency domain. The main process of VMD is given in Appendix A. Although the basic heartbeat signal is obtained after removing the respiration component, noise persists at frequencies near the normal heart rate. The VMD algorithm effectively decomposes the heartbeat signal into multiple IMFs in (A17). By selecting these IMFs from 1 to K based on the normal heartbeat frequency range, components that meet the frequency criteria are retained, while noise components outside this range are discarded. The index of each selected IMF is recorded as $s_1, s_2, \cdots, s_\beta$ where $1 \leqslant \beta \leqslant K$. The denoised heartbeat signal $\widetilde{H}[i]$ is obtained by summing the remaining components as shown below

$$\widetilde{H}[i] = \sum_{\gamma=1}^{\beta} u_{s_\gamma}[i] \tag{22}$$

After obtaining the denoised heartbeat signal $\widetilde{H}[i]$, the heart rate is estimated by transforming the signal into the frequency domain using the fast Fourier transform. The dominant frequency within the normal heart rate range is identified, and the heart rate is calculated as

$$\mathrm{HR} = 60 \times f_{\mathrm{peakHR}} \tag{23}$$

where f_{peakHR} denotes the dominant frequency component of the heartbeat signal, and 60 means 60 s for calculation.

The method presented in this section extracts the corresponding respiration and heartbeat signals.

4. Experimental Results

This section systematically details the experimental setup, validates the contribution of each proposed module, and conducts a comprehensive comparative analysis against state-of-the-art methods to evaluate the overall efficacy of the proposed method.

4.1. Experiment Settings

Experiments involved 16 volunteer subjects and the basic subject information is presented in Table 1. Each subject performed five separate trials under static, seated conditions. The mmWave radar system parameters are illustrated in Table 2. We activated antennas for transmitting Tx0 and for receiving Rx0-Rx3 to obtain the raw data during the experiment. Meanwhile, DCA1000EVM was transferring the raw data to the PC. Figure 2 shows the device including the radar system and ECG sensor. For ground-truth vital signs, a five-lead ECG sensor SPR9000B was attached to the subject's chest. The ECG sensor has a sampling rate of 40 Hz and provides heart rate and breath rate with an accuracy of ±1 bpm according to the manufacturer. The radar and ECG data were synchronized via software triggering. This study was conducted in accordance with the Declaration of Helsinki and approved by the Institutional Review Board (IRB) with approval No. H24257. All participants provided informed consent prior to data collection.

Table 1. Subject information.

Subject	Gender	Age (years)	Height (cm)	Weight (kg)
1	Male	25	170	60
2	Male	23	176	78
3	Male	23	172	70
4	Male	26	178	75
5	Male	54	170	72
6	Male	28	182	75
7	Male	31	172	74
8	Male	37	169	67
9	Female	22	158	49
10	Female	23	162	55
11	Female	23	161	45
12	Female	38	158	58
13	Female	26	156	43
14	Female	53	162	55
15	Female	24	160	50
16	Female	28	160	46

Table 2. Radar parameters.

Parameter	Value
Starting frequency	77 GHz
Frequency slope	70.006 MHz/μs
ADC sampling rate	4000 ksps
ADC samples	64
Valid signal bandwidth	1.1201 GHz
Number of frameas	4096
Slow time sampling period	12.5 ms
Antenna settings	Tx0 Rx0-Rx3

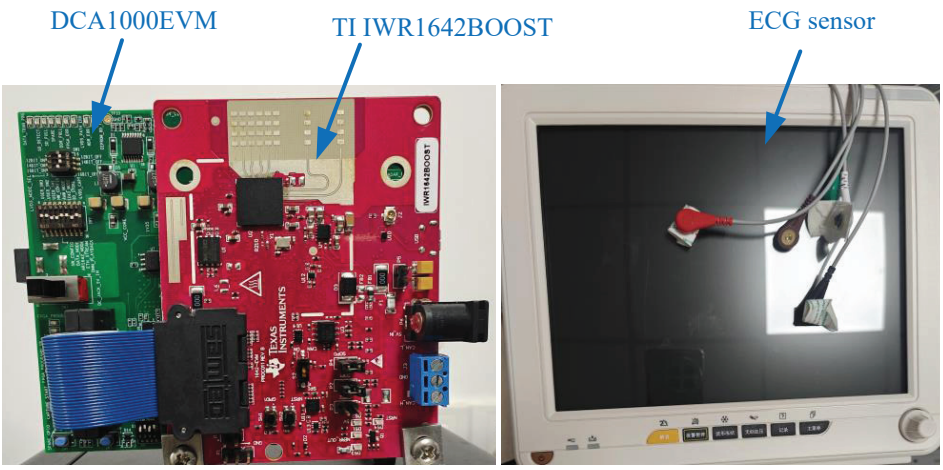

Figure 2. Radar system and ECG sensor.

The scenario of the experiment is shown in Figure 3. The Subject wears the ECG sensor on the chest and sits facing the radar at an approximate distance of 50–150 cm with normal breath and heartbeat. Measurement is conducted over a duration of 51.2s.

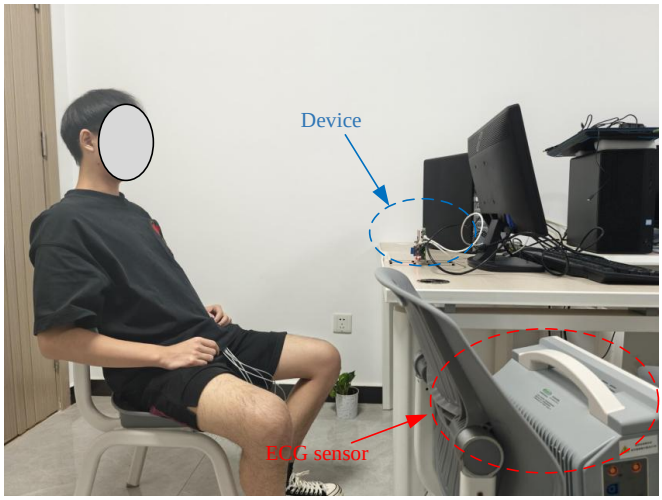

Figure 3. Experiment scenario.

4.2. Phase Correction Validation

Figure 4 presents the effectiveness of the phase correction method. As shown in Figure 4a, the Hampel-like filter successfully suppresses the outliers introduced by random body movements which helps reduce high-frequency interference. Additionally, the detrending process eliminates most low-frequency components as illustrated in Figure 4b.

The phase correction method is effective in reducing random noise and minimizing the influence of micro-movements caused by the human body compared to signals without it.

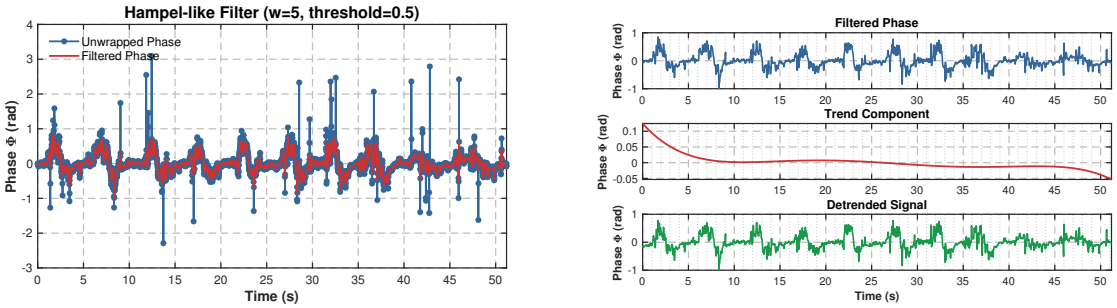

(a) **(b)**

Figure 4. Example of phase correction results: (**a**) shows the difference of unwrapped phase and filtered phase in time domain, and (**b**) demonstrates the function of signal detrending method.

4.3. Vital Signal Decomposition Based on APSVD and VMD-Denoising Validation

Additionally, to validate the effectiveness of signal decomposition in extracting the respiration signal and its harmonics, and heartbeat signals extraction, the method is applied to signal following phase correction.

4.3.1. Respiration Signal Extraction and Harmonics Suppression Validation

As shown in Figure 5a, the detrended signal has a main amplitude in 0.1–0.5 Hz, which is selected as P_r. Meanwhile, P_h is obtained from the relevant frequency domain. Then, the energy threshold η is obtained by (16), and j is calculated by (17). The respiration signal and its harmonics are extracted by utilizing the projection process as show in (18). Demonstrated in Figure 5b, the respiration frequency is remarkable, and the frequencies of harmonics are successfully decomposed. The heartbeat signal $H[i]$ has a more remarkable amplitude in the normal heartbeat frequency range compared to the detrended signal as shown in Figure 5c.

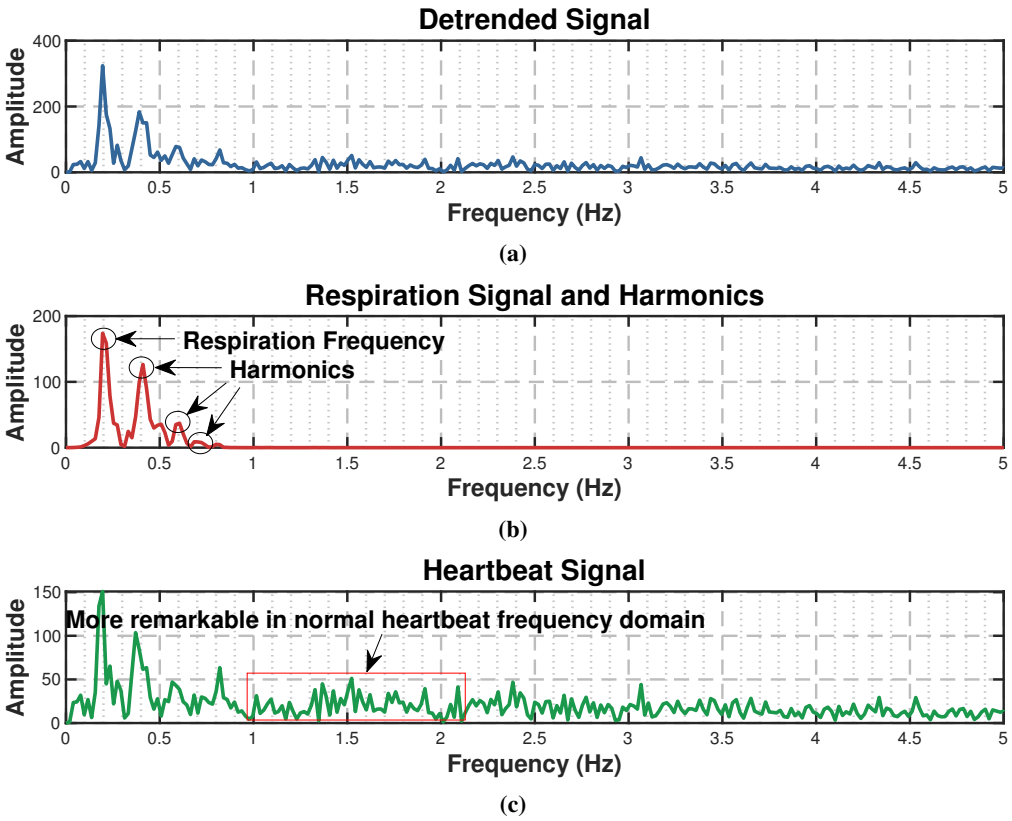

Figure 5. Example of APSVD. (**a**) shows the detrended signal in frequency domain, and (**b**) demonstrates the function of adaptive process in extracting respiration signal and its harmonics. (**c**) shows the heartbeat signal prepared for VMD-denoising method.

4.3.2. Heartbeat Signal Extraction Validation

The VMD-denoising method is used to extract the heartbeat signal with $K = 4$. Figures 6a,b illustrate the IMFs of the decomposed heartbeat signal obtained using the VMD algorithm. By filtering these IMFs based on normal heartbeat frequency, components that meet the criteria are retained, while those that do not are discarded.

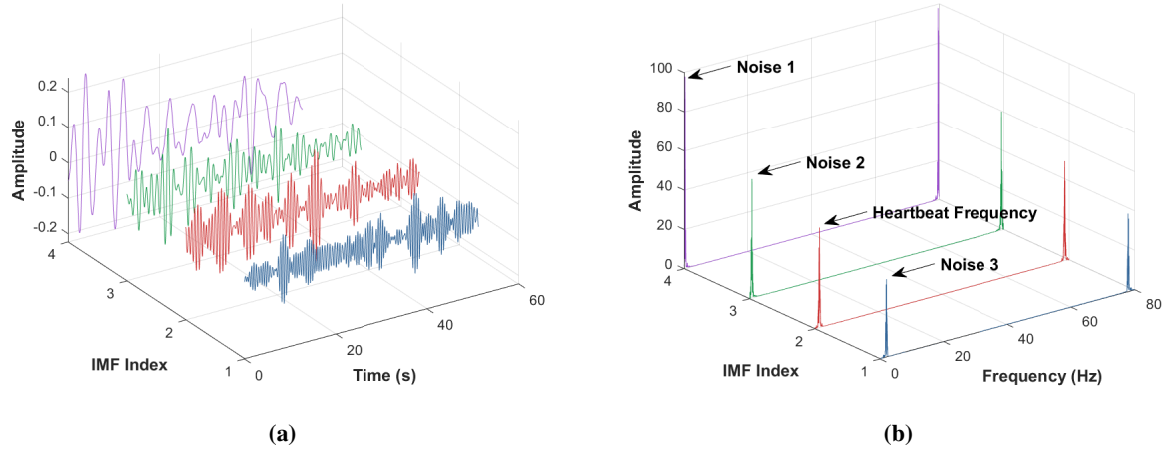

Figure 6. Example of VMD-denoising method. (**a**) IMFs of basic heartbeat signal in time domain and (**b**) shows the frequency domain.

Based on the validation results presented in this section, the proposed method effectively decomposes the mixed signal and extracts both respiration and heartbeat signals. The APSVD method successfully separates the respiration signal and its harmonics, as demonstrated in Figure 5, while the VMD-denoising method effectively isolates the heartbeat signal, as shown in Figure 6. Figure 7 shows the normalized signals. From these results, the vital signs can be separated from the mixed echo signal by the proposed method.

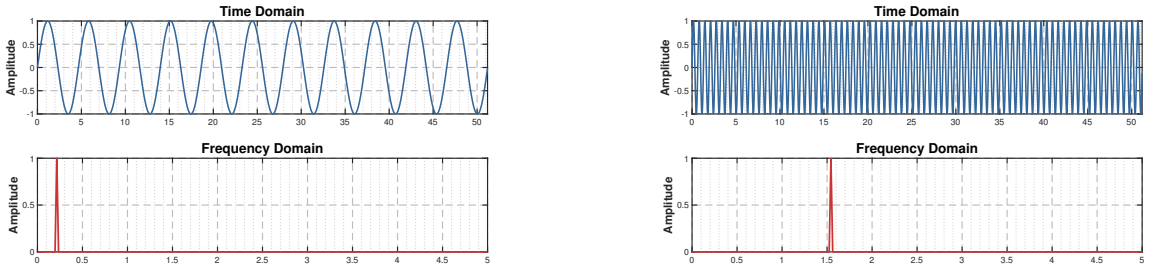

(a) **(b)**

Figure 7. Respiration and heartbeat signals obtained after normalization. (**a**) Respiration signal.(**b**) Heartbeat signal.

4.4. Comparison of other methods

This work studies a decomposition method for vital signals. The method separates heartbeat and respiration components from the mixed signal. Then breath rate (BR) and heart rate (HR) can be calculated.

The method is compared with four commonly used algorithms, including EEMD, CEEMDAN, VMD, and GWO-VMD.

Three metrics are used for evaluation. They are mean absolute error (MAE), mean relative error (MRE), and root mean square error (RMSE). These metrics are used for both HR and BR. They are defined as

$$\mathrm{MAE} = \frac{1}{n}\sum_{i=1}^{n}|y_i - \hat{y}_i| \tag{24}$$

$$\mathrm{MRE} = \frac{1}{n}\sum_{i=1}^{n}\left|\frac{y_i - \hat{y}_i}{y_i}\right| \tag{25}$$

$$\mathrm{RMSE} = \sqrt{\frac{1}{n}\sum_{i=1}^{n}(y_i - \hat{y}_i)^2} \tag{26}$$

Here, n is the total number of samples. y_i is the reference value of HR or BR obtained from the ECG sensor for the ith sample. $\hat{y}_i$ is the estimated value for the ith sample. In the following tables, MAE and RMSE are reported in bpm, whereas MRE is reported as a dimensionless ratio.

The results are shown in Table 3. They are also analyzed for respiration and heart rate in Tables 4 and 5. From these results, the proposed method keeps stable performance for both BR and HR. In some cases, the RMSE of HR is slightly higher. This is related to specific physiological conditions, which will be discussed later.

Table 3. Performance comparison of different algorithms.

Algorithms	BR			HR		
	MAE (bpm)	MRE	RMSE (bpm)	MAE (bpm)	MRE	RMSE (bpm)
EEMD	1.075949	0.109426	2.420901	4.871265	0.082308	6.537162
CEEMDAN	1.075949	0.109426	2.420901	4.868927	0.082266	6.532264
VMD	0.873418	0.079710	1.436416	5.086689	0.085719	6.732887
GWO-VMD	0.873418	0.079167	1.462614	4.876480	0.082311	6.526227
Proposed	1.063291	0.090903	1.550827	3.430380	0.057230	6.614139

4.4.1. Respiratory Signal Processing Capability

The results in Table 3 show the performance of different methods for respiratory signal decomposition. The proposed method has slightly higher MAE and MRE than VMD and GWO-VMD. Compared with EEMD and CEEMDAN, the proposed method reduces the BR-RMSE by approximately 35.9%. Although VMD and GWO-VMD obtain slightly lower aggregate BR-RMSE values, the proposed APSVD stage is designed not only for BR estimation but also for suppressing respiratory harmonics before HR extraction.

For Person15, the breathing pattern is irregular. As shown in Table 4, VMD and GWO-VMD achieve lower numerical BR errors for this subject, with MAE values of 0.2 bpm and 0.0 bpm, respectively. However, these results

should be interpreted carefully because a single rate-estimation metric mainly reflects the dominant frequency error and may not fully represent waveform-level fidelity under irregular respiration. The proposed method gives a slightly larger MAE of 1.0 bpm for Person15, but it preserves more respiratory fluctuation details after APSVD-based extraction. Therefore, the proposed method is not claimed to be the best in every individual BR case; rather, it provides a more balanced framework for respiratory harmonic suppression and subsequent HR extraction.

The increase in MAE and MRE is small. So it can be accepted in real applications. The proposed method keeps more details of the respiration signal. But VMD and GWO-VMD tend to smooth the signal to reduce average errors. Because of this, some small but important features may be lost. These features can be useful for detecting abnormal respiration conditions. Overall, the proposed method provides stable BR estimation while preserving respiratory components that are important for the subsequent removal of respiratory harmonics. Compared with methods that directly decompose the mixed signal, the proposed APSVD-based strategy explicitly extracts the respiration component and its harmonics before HR estimation. This design explains why the method is particularly useful in the complete BR/HR separation framework, even though VMD-based methods may obtain lower BR errors in some individual cases.

4.4.2. Superiority of APSVD and VMD-Denoising in Heart Rate Estimation

As shown in Table 5, the proposed method achieves the best HR-MAE and HR-MRE for most subjects, indicating its advantage in reducing average HR estimation error. However, as shown in Table 3, its overall HR-RMSE is slightly higher than those of EEMD, CEEMDAN, and GWO-VMD because RMSE is more sensitive to several motion-contaminated outliers. For 12 subjects (e.g., Person1, Person3, Person5), the proposed method reduces MAE by 50–75% compared to conventional methods. Particularly for Person11, it achieves MAE 3.2 bpm versus 11.077 bpm for EEMD, achieving a 71.1% improvement. While the proposed method shows slightly higher HR-RMSE in Table 3, this stems from only two cases: The RMSE of Person8 is 19.799 bpm, and the RMSE of Person16 is 12.052 bpm. The relatively high HR-RMSE mainly comes from two motion-contaminated cases: Person8 and Person16, whose RMSE values are 19.799 bpm and 12.052 bpm, respectively. Retrospective inspection of the radar phase signals indicates that these two cases contain noticeable body micro-movements and transient phase jumps during data acquisition. Although the Hampel-like filter suppresses abrupt points to some extent, residual nonlinear motion artifacts may still remain and interfere with the VMD-based selection of heartbeat-related IMFs. Therefore, these results reveal a current limitation of the proposed method under non-stationary body motion rather than a general failure of the decomposition framework. The interquartile range of HR-MAE for the proposed method is 1.8–3.8 bpm. This range is 60% narrower than that of EEMD, which is 3.4–6.6 bpm. So the proposed method shows more stable performance across different subjects.

Table 4. Performance comparison of breath rate estimation.

Subject	EEMD			CEEMDAN			VMD			GWO-VMD			Proposed		
	MAE (bpm)	MRE	RMSE (bpm)	MAE (bpm)	MRE	RMSE (bpm)	MAE (bpm)	MRE	RMSE (bpm)	MAE (bpm)	MRE	RMSE (bpm)	MAE (bpm)	MRE	RMSE (bpm)
Person1	0.1	0.008	0.223	0.1	0.008	0.223	0.1	0.008	0.223	0.1	0.008	0.223	**0.9**	**0.082**	**1.024**
Person2	0.4	0.036	0.547	0.4	0.036	0.547	0.4	0.036	0.547	0.4	0.036	0.547	**0.8**	**0.070**	**0.948**
Person3	2.1	0.099	2.598	2.1	0.099	2.598	1.3	0.061	1.396	1.3	0.061	1.396	**1.9**	**0.090**	**2.179**
Person4	1.4	0.066	1.516	1.4	0.066	1.516	1.4	0.066	1.516	1.4	0.066	1.516	**1.6**	**0.074**	**1.923**
Person5	0.3	0.026	0.387	0.3	0.026	0.387	0.3	0.026	0.387	0.3	0.026	0.387	**0.5**	**0.043**	**0.741**
Person6	0.4	0.041	0.447	0.4	0.041	0.447	0.4	0.041	0.447	0.4	0.041	0.447	**0.4**	**0.041**	**0.447**
Person7	0.6	0.030	1.000	0.6	0.030	1.000	0.6	0.030	1.000	0.6	0.030	1.000	**0.6**	**0.033**	**1.341**
Person8	1.0	0.089	1.843	1.0	0.089	1.843	0.8	0.069	1.414	1.0	0.089	1.843	**0.6**	**0.049**	**1.000**
Person9	1.1	0.110	1.118	1.1	0.110	1.118	1.1	0.110	1.118	1.1	0.110	1.118	**1.1**	**0.110**	**1.118**
Person10	1.0	0.104	1.183	1.0	0.104	1.183	1.6	0.164	2.097	1.6	0.164	2.097	**1.0**	**0.104**	**1.183**
Person11	0.6	0.024	0.774	0.6	0.024	0.774	0.6	0.024	0.774	0.6	0.024	0.774	**0.8**	**0.036**	**1.095**
Person12	1.2	0.051	1.673	1.2	0.051	1.673	1.2	0.051	1.673	1.2	0.051	1.673	**2.4**	**0.102**	**2.966**
Person13	0.6	0.067	0.774	0.6	0.067	0.774	0.6	0.067	0.774	0.6	0.067	0.774	**0.4**	**0.042**	**0.632**
Person14	0.8	0.096	0.894	0.8	0.096	0.894	0.8	0.096	0.894	0.8	0.096	0.894	**1.2**	**0.176**	**1.897**
Person15	3.6	0.600	8.049	3.6	0.600	8.049	0.2	0.028	0.447	0.0	0.000	0.000	**1.0**	**0.142**	**1.183**
Person16	2.25	0.345	2.783	2.25	0.345	2.783	3.0	0.470	4.183	3.0	0.470	4.183	**2.0**	**0.295**	**2.738**

Table 5. Performance comparison of heart rate estimation.

Subject	EEMD			CEEMDAN			VMD			GWO-VMD			Proposed		
	MAE (bpm)	MRE	RMSE (bpm)	MAE (bpm)	MRE	RMSE (bpm)	MAE (bpm)	MRE	RMSE (bpm)	MAE (bpm)	MRE	RMSE (bpm)	MAE (bpm)	MRE	RMSE (bpm)
Person1	10.395	0.186	11.118	10.360	0.185	11.082	10.398	0.186	11.119	10.172	0.182	10.972	**2.900**	**0.051**	**4.201**
Person2	3.821	0.063	4.688	3.820	0.063	4.673	3.790	0.063	4.659	3.804	0.063	4.676	**2.800**	**0.047**	**3.302**
Person3	3.978	0.063	4.063	3.972	0.063	4.055	3.971	0.063	4.057	4.023	0.064	4.112	**1.800**	**0.028**	**2.324**
Person4	6.603	0.106	7.127	6.610	0.106	7.127	6.598	0.105	7.129	6.385	0.102	6.754	**3.000**	**0.049**	**3.493**
Person5	3.437	0.052	3.833	3.437	0.052	3.833	4.012	0.061	4.442	3.515	0.053	4.084	**1.800**	**0.027**	**1.949**
Person6	4.893	0.080	7.758	4.892	0.080	7.758	5.271	0.086	7.910	4.907	0.078	6.531	**3.200**	**0.052**	**5.550**
Person7	1.125	0.019	1.346	1.125	0.019	1.346	1.130	0.019	1.350	1.163	0.020	1.409	**0.400**	**0.007**	**0.894**
Person8	6.453	0.113	8.399	6.453	0.113	8.399	6.295	0.111	8.334	6.268	0.110	8.615	**15.600**	**0.274**	**19.799**
Person9	3.704	0.054	4.051	3.704	0.054	4.051	3.712	0.054	4.050	3.946	0.057	4.158	**1.100**	**0.015**	**1.285**
Person10	4.177	0.064	4.900	4.177	0.064	4.900	4.482	0.069	5.371	3.535	0.055	5.816	**3.800**	**0.055**	**6.017**
Person11	11.077	0.213	13.278	11.077	0.213	13.278	11.067	0.213	13.271	10.444	0.202	12.580	**3.200**	**0.056**	**4.775**
Person12	2.398	0.041	3.163	2.398	0.041	3.163	2.491	0.043	3.206	3.187	0.054	3.689	**1.600**	**0.027**	**1.673**
Person13	2.869	0.043	3.586	2.869	0.043	3.586	3.755	0.057	4.920	1.707	0.026	1.946	**2.000**	**0.030**	**2.098**
Person14	5.013	0.084	5.784	5.013	0.084	5.784	6.908	0.115	7.226	5.154	0.087	5.707	**3.800**	**0.064**	**5.348**
Person15	3.692	0.063	4.181	3.692	0.063	4.181	3.172	0.053	4.193	4.900	0.081	5.845	**1.800**	**0.029**	**2.236**
Person16	4.163	0.071	5.541	4.163	0.071	5.541	4.147	0.070	5.525	4.920	0.084	6.994	**6.750**	**0.114**	**12.052**

5. Conclusions

In this paper, a vital sign decomposition framework for FMCW mmWave radar is studied. The framework combines phase correction, APSVD, and VMD-based denoising. It is used to separate respiration, respiratory harmonics, and heartbeat signals under practical conditions.

The phase correction part includes phase unwrapping, phase difference, abrupt change suppression, and signal detrending. These steps improve the signal quality compared with the raw signal. Then APSVD and VMD-denoising are used together to reduce harmonic interference and avoid manual parameter adjustment. For the 16 subjects in the experiments, the proposed method achieves a BR-MAE of 1.063291 bpm, a BR-MRE of 0.090903, and a BR-RMSE of 1.550827 bpm. For HR estimation, it achieves an HR-MAE of 3.430380 bpm, an HR-MRE of 0.057230, and an HR-RMSE of 6.614139 bpm. Compared with EEMD, CEEMDAN, VMD, and GWO-VMD, the proposed method shows clear advantages in HR-MAE and HR-MRE, while maintaining competitive RMSE performance.

The proposed framework has also been implemented on the ADT3102 radar chip. Under relatively still conditions, the system outputs respiration rate and heart rate every 12.8 s. It also includes human presence detection and abnormal respiration detection, which improves its practical use. But the 12.8 s update interval is still long for some tasks with high real-time requirements. Also, the method still depends on subject stillness. Large body movements can reduce the estimation accuracy.

Future work will continue in two directions. One is to reduce latency by using pipeline processing and frame overlapping, so that the output interval can be shortened to less than 10 s. The other is to extend the method to movement scenarios. For this purpose, a motion-tolerant framework will be developed by combining motion detection and deep learning-based artifact suppression. In this way, the limit caused by the stillness requirement can be reduced.

Author Contributions

Y.H.: conceptualization, formal analysis, investigation, methodology, software, writing—original draft preparation, writing—review and editing; D.L.: data curation, formal analysis, investigation, validation, visualization; J.C.: investigation, software, resources; H.F.: data curation, investigation, validation; J.Y.: data curation, supervision; J.Z.: visualization; S.L.: writing—review and editing; M.D.: project administration, writing—review and editing; Z.W.: supervision, resources, funding acquisition, writing—review and editing; Y.W.: project administration, resources; H.L.: supervision, funding acquisition, project administration, resources, writing—review and editing. All authors have read and agreed to the published version of the manuscript.

Funding

This research was funded by the Fundamental Research Funds for the Central Universities, grant numbers SWU-XDJH202312 and SWU-KQ24042; the National Natural Science Foundation of China, grant numbers 62173278 and 62403394; the Chongqing Science Fund for Distinguished Young Scholars, grant number 2024NSCQ-JQX0103; and the Innovation Support Program for Chongqing Overseas Returnees, grant number cx2024048.

Institutional Review Board Statement

The study was conducted according to the guidelines of the Declaration of Helsinki, and approved by the Institutional Review Board of Southwest University (protocol code H24257 and date of approval: December 7, 2024).

Informed Consent Statement

Informed consent was obtained from all subjects involved in the study.

Data Availability Statement

The data are not publicly available due to privacy restrictions.

Conflicts of Interest

The authors declare no conflict of interest.

Use of AI and AI-Assisted Technologies

During the preparation of this work, the authors used AI-assisted tools for language editing and grammar improvement. After using these tools, the authors carefully reviewed and revised the content and take full responsibility for the final manuscript.

Appendix A. Mixed Signal Model

The complete data acquisition and signal processing flow are depicted in Figure A1. After data capture, the fast Fourier transform (FFT) is applied along the fast-time dimension to locate the target range bin.

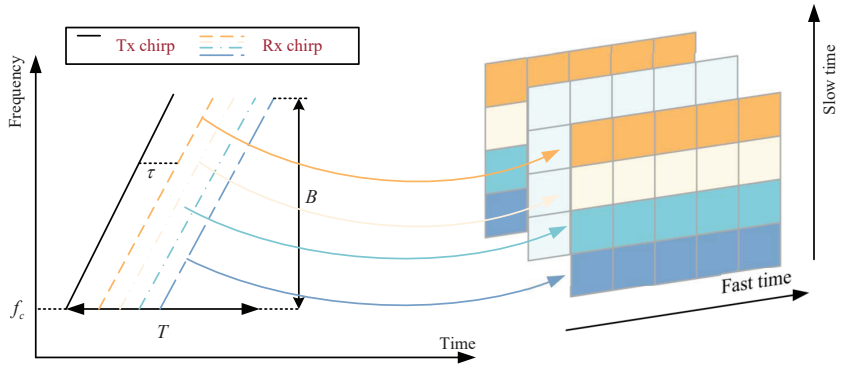

Figure A1. Data acquisition and signal processing procedures of the mmWave radar system.

The FMCW radar transmits a chirp signal whose frequency increases linearly with time [35]. The instantaneous transmit frequency is

$$f_{\mathrm{T}}(t) = f_c + \frac{B}{T}t \tag{A1}$$

where f_c is the start frequency, B is the bandwidth, and T is the chirp duration. The transmit phase is

$$\phi_{\mathrm{T}}(t) = 2\pi \int_0^t f_{\mathrm{T}}(\tau)\, d\tau = 2\pi \left(f_c t + \frac{1}{2}\frac{B}{T}t^2 \right) \tag{A2}$$

The transmitted FMCW signal is a real-valued signal and can be expressed as

$$s_T(t) = A\cos\left(2\pi f_c t + \pi \frac{B}{T}t^2\right) \tag{A3}$$

After I/Q demodulation, the received signal can be represented in complex form for signal processing convenience. Thus, the transmit signal can be written as

$$s_{\mathrm{T}}(t) = A_1(t)e^{-j\left[2\pi\left(f_c t + \frac{1}{2}\frac{B}{T}t^2\right) + \varphi(t)\right]} \tag{A4}$$

where $A_1(t)$ is the amplitude and $\varphi(t)$ represents hardware phase noise.

Assuming a stationary object at distance R_0, the received signal is a delayed version

$$s_{\mathrm{R}}(t) = A_2(t)e^{-j\left[2\pi\left(f_c(t-\tau)+\frac{1}{2}\frac{B}{T}(t-\tau)^2\right)+\varphi(t-\tau)\right]} \tag{A5}$$

where $A_2(t)$ is the amplitude of the received signal, with time delay $\tau = 2R_0/c$(c:speed of light). Mixing the received signal with a copy of the transmit signal yields the intermediate frequency (IF) signal

$$Y(t) = Ae^{-j\left[2\pi\frac{B}{T}\tau\, t+2\pi f_c\tau+\pi\frac{B}{T}\tau^2+\Delta\varphi(t)\right]} \tag{A6}$$

where $\Delta\varphi(t) = \varphi(t) - \varphi(t-\tau)$ is the residual phase noise, which is typically negligible due to the range correlation effect [35]. The term $\pi\frac{B}{T}\tau^2$ is very small for short-range applications and can be ignored. Hence,

$$Y(t) \approx Ae^{-j(2\pi ft+\phi)}, \quad \text{with } f = \frac{B}{T}\tau = \frac{2BR_0}{cT}, \quad \phi = 2\pi f_c\tau. \tag{A7}$$

When the target is a human chest, the distance $R(t)$ is not constant but varies due to respiration and heartbeat

$$R(t) = R_0 + R_c(t) \tag{A8}$$

where $R_c(t)$ represents the chest displacement caused by cardiopulmonary activity. The phase then becomes time-varying

$$\phi(t) = \frac{4\pi}{\lambda}R(t) = \frac{4\pi}{\lambda}\left(R_0 + R_c(t)\right) \tag{A9}$$

with $\lambda = c/f_c$ the wavelength.

After I/Q sampling, the discrete-time IF signal for the n-th ADC sample (fast time) and m-th chirp (slow time) is

$$Y[n,m] = Ae^{-j\left(2\pi fnT_f+\frac{4\pi}{\lambda}R(nT_f+mT_s)\right)} \tag{A10}$$

where T_f is the fast-time sampling interval, T_s is the slow-time sampling interval, $n = 1,\ldots,N$, and $m = 1,\ldots,M$. The slow-time samples contain the vital sign information.

Appendix B. Variational Mode Decomposition Theory

Variational mode decomposition (VMD) is an adaptive signal decomposition technique that decomposes a signal into a predefined number of band-limited intrinsic mode functions (IMFs). Each mode is compact around a specific center frequency and represents a distinct spectral component of the signal.

1. Variational Formulation

Given an input signal $f(t)$, VMD aims to decompose it into K modes $\{u_k(t)\}_{k=1}^K$, each associated with a center frequency $\{\omega_k\}_{k=1}^K$. The objective is to minimize the total bandwidth of all modes under the constraint that their sum reconstructs the original signal.

The variational problem is formulated as

$$\min_{\{u_k\},\{\omega_k\}} \sum_{k=1}^{K} \left\|\partial_t\left[u_k(t)e^{-j\omega_k t}\right]\right\|_2^2 \tag{A11}$$

subject to

$$\sum_{k=1}^{K} u_k(t) = f(t) \tag{A12}$$

In this formulation, each mode $u_k(t)$ is first demodulated to baseband via $e^{-j\omega_k t}$, and its bandwidth is estimated using the squared L_2 norm of the gradient.

2. Augmented Lagrangian and ADMM Solution

The constrained optimization problem is solved by introducing the augmented Lagrangian

$$\mathcal{L}(\{u_k\},\{\omega_k\},\lambda) = \alpha\sum_{k=1}^{K}\left\|\partial_t\left[u_k(t)e^{-j\omega_k t}\right]\right\|_2^2 + \left\|f(t) - \sum_{k=1}^{K}u_k(t)\right\|_2^2 + \left\langle \lambda(t), f(t) - \sum_{k=1}^{K}u_k(t)\right\rangle \tag{A13}$$

Here, $\lambda(t)$ is the Lagrange multiplier and α is the penalty parameter.

Then the alternating direction method of multipliers (ADMM) is used to solve this problem. In each iteration, the mode u_k, the center frequency ω_k, and the Lagrange multiplier λ are updated in turn.

3. Frequency-Domain Updates

In the frequency domain, each mode is updated as

$$\hat{u}_k(\omega) = \frac{\hat{f}(\omega) - \sum_{i \neq k} \hat{u}_i(\omega) + \frac{\hat{\lambda}(\omega)}{2}}{1 + 2\alpha(\omega - \omega_k)^2} \tag{A14}$$

The center frequency is updated as

$$\omega_k = \frac{\int_0^\infty \omega |\hat{u}_k(\omega)|^2 d\omega}{\int_0^\infty |\hat{u}_k(\omega)|^2 d\omega} \tag{A15}$$

The Lagrange multiplier is updated as

$$\lambda^{n+1}(t) = \lambda^n(t) + \tau \left(f(t) - \sum_{k=1}^{K} u_k(t) \right) \tag{A16}$$

where τ is the update step size.

4. Application in Heartbeat Signal Extraction

In this study, VMD is applied to the residual signal after the respiration component is removed. The signal is decomposed into K modes. Each mode corresponds to one frequency band.

Then the IMFs with center frequencies in the physiological heart-rate range are selected. The denoised heartbeat signal is reconstructed by summing these selected modes

$$\widetilde{H}[i] = \sum_{\gamma=1}^{\beta} u_{s_\gamma}[i] \tag{A17}$$

where u_{s_γ} denotes the selected IMFs and β is the number of retained modes.

In this way, noise components outside the heartbeat frequency band are reduced. So the heartbeat signal can be extracted more accurately.

References

1. Al-Mahmud, O.; Khan, K.; Roy, R.; et al. Internet of Things (IoT) Based Smart Health Care Medical Box for Elderly People. In Proceedings of the 2020 International Conference for Emerging Technology (INCET), Belgaum, India, 5–7 June 2020. .
2. Liao, C.; Shay, O.; Gomes, E.; et al. Noninvasive Continuous Blood Pressure Measurement with Wearable Millimeter Wave Device. In Proceedings of the 2021 IEEE 17th International Conference on Wearable and Implantable Body Sensor Networks (BSN), Athens, Greece, 27–30 July 2021. https://doi.org/10.1109/BSN51625.2021.9507020
3. Yang, X.; Fan, D.; Ren, A.; et al. Sleep Apnea Syndrome Sensing at C-Band. *IEEE J. Transl. Eng. Health Med.* **2018**, *6*, 2701008. https://doi.org/10.1109/JTEHM.2018.2879085
4. Zhao, X.; Wang, W.; Li, C.; et al. Diagnosis of Sleep Apnea Hypopnea Syndrome Using Fusion of Micro-Motion Signals from Millimeter-Wave Radar and Pulse Wave Data. *J. Radars* **2025**, *14*, 102–116. https://doi.org/10.12000/JR24107
5. Gianoglio, C.; Mohanna, A.; Rizik, A.; et al. On Edge Human Action Recognition Using Radar-Based Sensing and Deep Learning. *IEEE Trans. Ind. Inform.* **2024**, *20*, 4160–4172.
6. Thornburg, A.; Bai, T.; Heath, R.W. Performance Analysis of Outdoor mmWave Ad Hoc Networks. *IEEE Trans. Signal Process.* **2016**, *64*, 4065–4079.
7. Dai, T.K.V.; Oleksak, K.; Kvelashvili, T.; et al. Enhancement of Remote Vital Sign Monitoring Detection Accuracy Using Multiple-Input Multiple-Output 77 GHz FMCW Radar. *IEEE J. Electromagn. Microwaves Med. Biol.* 2022, 6, 111–122. https://doi.org/10.1109/JERM.2021.3082807.
8. Li, C.; Lubecke, V.; Boric-Lubecke, O.; et al. Sensing of Life Activities at the Human-Microwave Frontier. *IEEE J. Microwaves* **2021**, *1*, 66–78.
9. Ma, L.; Wang, Z.; Fan, J.; et al. Interpretation of Report on Cardiovascular Health and Diseases in China 2022. *Chin. Gen. Pract.* **2023**, *26*, 3975–3994. (In Chinese)
10. Xu, C.; Hu, N.; Li, Y. A Millimeter Wave Radar Target Detection Method in K-Distributed Clutter Background. In

Proceedings of the 2021 IEEE Conference on Telecommunications, Optics and Computer Science (TOCS), Shenyang, China, 10–11 December 2021; pp. 489–493. https://doi.org/10.1109/TOCS53301.2021.9688689.

11. Liu, J.; Li, Y.; Li, C.; et al. Accurate Measurement of Human Vital Signs with Linear FMCW Radars under Proximity Stationary Clutters. *IEEE Trans. Biomed. Circuits Syst.* **2021**, *15*, 1393–1404. https://doi.org/10.1109/TBCAS.2021.3123830.
12. Wang, G.; Munoz-Ferreras, J.-M.; Gu, C.; et al. Application of Linear-Frequency-Modulated Continuous-Wave (LFMCW) Radars for Tracking of Vital Signs. *IEEE Trans. Microw. Theory Tech.* **2014**, *62*, 1387–1399. https://doi.org/10.1109/TMTT.2014.2320464.
13. Ayhan, S.; Scherr, S.; Bhutani, A.; et al. Impact of Frequency Ramp Nonlinearity, Phase Noise, and SNR on FMCW Radar Accuracy. *IEEE Trans. Microw. Theory Tech.* **2016**, *64*, 3290–3301. https://doi.org/10.1109/TMTT.2016.2599165
14. Paterniani, G.; Sgreccia, D.; Davoli, A.; et al. Radar-Based Monitoring of Vital Signs: A Tutorial Overview. *Proc. IEEE* **2023**, *111*, 277–317. https://doi.org/10.1109/JPROC.2023.3244362.
15. Li, C.; Peng, Z.; Huang, T.; et al. A Review on Recent Progress of Portable Short-Range Noncontact Microwave Radar Systems. *IEEE Trans. Microw. Theory Tech.* **2017**, *65*, 1692–1706. https://doi.org/10.1109/TMTT.2017.2650911.
16. Ni, Z.; Huang, B. Open-Set Human Identification Based on Gait Radar Micro-Doppler Signatures. *IEEE Sensors J.* **2021**, *21*, 8226–8233. https://doi.org/10.1109/JSEN.2021.3052613.
17. Dang, X.; Zhang, J.; Hao, Z. A Non-Contact Detection Method for Multi-Person Vital Signs Based on IR-UWB Radar. *Sensors* **2022**, *22*, 6116.
18. Sadreazami, H.; Bolic, M.; Rajan, S. Fall Detection Using Standoff Radar-Based Sensing and Deep Convolutional Neural Network. *IEEE Trans. Circuits Syst. II Express Briefs* **2020**, *67*, 197–201. https://doi.org/10.1109/TCSII.2019.2904498.
19. Zhang, F.; Wang, Z.; Jin, B.; et al. Your Smart Speaker Can "Hear" Your Heartbeat! *Proc. ACM Interact. Mob. Wearable Ubiquitous Technol.* **2020**, *4*, 1–24. https://doi.org/10.1145/3432237.
20. Xu, Z.; Shi, C.; Zhang, T.; et al. Simultaneous Monitoring of Multiple People's Vital Sign Leveraging a Single Phased-MIMO Radar. *IEEE J. Electromagn. Microwaves Med. Biol.* **2022**, *6*, 311–320. https://doi.org/10.1109/JERM.2022.3143431.
21. Fang, Z.; Jian, P.; Zhang, H.; et al. Review of Noncontact Medical and Health Monitoring Technologies Based on FMCW Radar. *J. Radars* **2022**, *11*, 499–516. https://doi.org/10.12000/JR22019 (In Chinese)
22. Bae, C.; Lee, S.; Jung, Y. High-Speed Continuous Wavelet Transform Processor for Vital Signal Measurement Using Frequency-Modulated Continuous Wave Radar. *Sensors* **2022**, *22*, 3073.
23. Seena, V.; Yomas, J. A Review on Feature Extraction and Denoising of ECG Signal Using Wavelet Transform. In Proceedings of the 2nd International Conference on Devices, Circuits and Systems (ICDCS), Coimbatore, India, 6–8 March 2014. https://doi.org/10.1109/ICDCSyst.2014.6926190.
24. Wu, Y.; Ni, H.; Mao, C.; et al. Contactless Reconstruction of ECG and Respiration Signals with mmWave Radar Based on RSSRnet. *IEEE Sensors J.* **2024**, *24*, 6358–6368. https://doi.org/10.1109/JSEN.2023.3333025.
25. Wang, H.; Du, F.; Zhu, H.; et al. HeRe: Heartbeat Signal Reconstruction for Low-Power Millimeter-Wave Radar Based on Deep Learning. *IEEE Trans. Instrum. Meas.* **2023**, *72*, 4004515. https://doi.org/10.1109/TIM.2023.3267348.
26. Bauder, C.; Moadi, A.-K.; Rajagopal, V.; et al. mm-MuRe: mmWave-Based Multi-Subject Respiration Monitoring via End-to-End Deep Learning. *IEEE J. Electromagn. Microwaves Med. Biol.* **2025**, *9*, 49–61. https://doi.org/10.1109/JERM.2024.3443782.
27. Strodthoff, N.; Wagner, P.; Schaeffter, T.; et al. Deep Learning for ECG Analysis: Benchmarks and Insights from PTB-XL. *IEEE J. Biomed. Health Inform.* **2021**, *25*, 1519–1528. https://doi.org/10.1109/JBHI.2020.3022989.
28. Xu, D.; Yu, W.; Deng, C.; et al. Non-Contact Detection of Vital Signs Based on Improved Adaptive EEMD Algorithm. *Sensors* **2022**, *22*, 6423.
29. Yan, J.; Hong, H.; Zhao, H.; et al. Through-Wall Multiple Targets Vital Signs Tracking Based on VMD Algorithm. *Sensors* **2016**, *16*, 1293. https://doi.org/10.3390/s16081293.
30. Wang, F.; Zeng, X.; Wu, C.; et al. mmHRV: Contactless Heart Rate Variability Monitoring Using Millimeter-Wave Radio. *IEEE Internet Things J.* **2021**, *8*, 16623–16636. https://doi.org/10.1109/JIOT.2021.3075167.
31. Wu, Z.; Huang, N. Ensemble Empirical Mode Decomposition: A Noise-Assisted Data Analysis Method. *Adv. Data Sci. Adapt. Anal.* **2009**, *1*, 1–41. https://doi.org/10.1142/S1793536909000047.
32. Torres, M.; Colominas, M.; Schlotthauer, G.; et al. A Complete Ensemble Empirical Mode Decomposition with Adaptive Noise. In Proceedings of the IEEE International Conference on Acoustics, Speech and Signal Processing (ICASSP), Prague, Czech Republic, 22–27 May 2011; pp. 4144–4147. https://doi.org/10.1109/ICASSP.2011.5947265.
33. Dragomiretskiy, K.; Zosso, D. Variational Mode Decomposition. *IEEE Trans. Signal Process.* **2014**, *62*, 531–544. https://doi.org/10.1109/TSP.2013.2288675.
34. Wang, Y.; Markert, R.; Xiang, J.; et al. Research on Variational Mode Decomposition and Its Application in Detecting Rub-Impact Fault of the Rotor System. *Mech. Syst. Signal Process.* **2015**, *60–61*, 243–251. https://doi.org/10.1016/j.ymssp.2015.02.020.
35. Ahmad, A.; Roh, J.; Wang, D.; et al. Vital Signs Monitoring of Multiple People Using a FMCW Millimeter-Wave Sensor. In Proceedings of the IEEE Radar Conference (RadarConf18), Oklahoma City, OK, USA, 23–27 April 2018; pp. 1450–1455. https://doi.org/10.1109/RADAR.2018.8378778.
36. IWR1642 BoosterPack Evaluation Module for Single-Chip 77GHz mmWave sensor. Available online: https://www.ti.com/tool/IWR1642BOOST (accessed on 19 May 2020) .

37. DCA1000 Evaluation Module for Real-Time Data Capture and Streaming. Available online: https://www.ti.com/tool/DCA1000EVM (accessed on 1 February 2019).
38. Kang, D.; Ming, X.; Xiaofei, Z. Phase Difference Correction Method for Phase and Frequency in Spectral Analysis. *Mech. Syst. Signal Process.* **1999**, *14*, 835–843.
39. Qu, L.; Liu, C.; Yang, T.; et al. Vital Sign Detection of FMCW Radar Based on Improved Adaptive Parameter Variational Mode Decomposition. *IEEE Sensors J.* **2023**, *23*, 25048–25060. https://doi.org/10.1109/JSEN.2023.3312513.
40. Bhowmik, S.; Jelfs, B.; Arjunan, S.P.; et al. Outlier Removal in Facial Surface Electromyography through Hampel Filtering Technique. In Proceedings of the IEEE Life Sciences Conference (LSC), Sydney, NSW, Australia, 13–15 December 2017; pp. 258–261. https://doi.org/10.1109/LSC.2017.8268192.
41. Wall, M.E.; Rechtsteiner, A.; Rocha, L.M. Singular Value Decomposition and Principal Component Analysis. In *A Practical Approach to Microarray Data Analysis*; Berrar, D.P., Dubitzky, W., Granzow, M., Eds.; Springer: Boston, MA, USA, 2003; pp. 91–109.
42. American Heart Association. All About Heart Rate (Pulse). Available online: https://www.heart.org/en/health-topics/high-blood-pressure/the-facts-about-high-blood-pressure/all-about-heart-rate-pulse (accessed on 13 May 2024).